



Investigation on the optimization, design and microwave absorption properties of BaTb_{0.2}Eu_{0.2}Fe_{11.6}O₁₉/PANI decorated on reduced graphene oxide nanocomposites

Juhua Luo^{1,2,*} , Lu Yue², Hongru Ji¹, Kang Zhang¹, and Ning Yu¹

¹School of Materials Science and Engineering, Yancheng Institute of Technology, Yancheng 224051, China

²Key Laboratory for Advanced Technology in Environmental Protection of Jiangsu Province, Yancheng Institute of Technology, Yancheng 224051, China

Received: 4 October 2018

Accepted: 28 December 2018

Published online:

7 January 2019

© Springer Science+Business Media, LLC, part of Springer Nature 2019

ABSTRACT

A novel hybrid material with excellent microwave absorption property has been designed by decorating reduced graphene oxide with Ba Tb_{0.2}Eu_{0.2}Fe_{11.6}O₁₉/PANI composite, and the effect of graphene content on microwave absorption property has been investigated. The microstructure of the composite is characterized by X-ray diffraction, Fourier-transform infrared spectroscopy, field emission scanning electron microscope, transmission electron microscope and Raman spectroscopy. The mechanism of microwave absorption is discussed minutely. The result shows that the ternary nanocomposites demonstrate unexceptionable microwave absorption property due to its special nanostructures and synergistic effect among BaTb_{0.2}Eu_{0.2}Fe_{11.6}O₁₉, PANI and RGO. The minimum reflection loss can reach – 60.9 dB at 16.4 GHz with a thickness of only 1.95 mm, and the corresponding effective absorption bandwidth (below – 10 dB) is 4.2 GHz. BaTb_{0.2}Eu_{0.2}Fe_{11.6}O₁₉/PANI/RGO composite can be one of the most promising microwave absorption materials.

Introduction

Recently, to protect biological systems and electronic equipment against potential damages to electromagnetic (EM) contamination, especially caused by the explosive utilization of gigahertz EM waves, a functional material with low density, strong absorption, thin thickness and wide absorption frequency range

is intensively pursued [1–3]. Nowadays, researchers attempted to study all kinds of materials which can absorb EM wave by converting electromagnetic energy into thermal energy or dissipating them through interference, which depends on their dielectric or magnetic loss ability [4]. The balance of permittivity and permeability, which is named as EM wave impedance matching, is beneficial for

Address correspondence to E-mail: luojuhua@163.com

enhancing the EM wave absorbing capability [5]. Therefore, the conjugation of dielectric materials and magnetic materials has attracted tremendous attention in electromagnetic pollution applications.

Traditionally, M-type ferrites are considered to be the best choice for EM wave absorber among magnetic microwave absorbers for their remarkable advantages, such as low cost and strong magnetic loss performances at high-frequency range [6]. Moreover, electromagnetic properties of barium ferrites can be improved by substitution of Fe^{3+} with rare earth cations, such as La^{3+} , Ce^{3+} and Zr^{4+} . [7–10]. For instance, Li et al. [11] studied Co^{2+} – Zr^{4+} co-doped barium ferrite ceramics; the results showed that the maximum reflection loss can reach about -28.7 dB at 16.4 GHz and presented a broad effective bandwidth of 5.46 GHz (from 13.34 to 18.8 GHz) with a thickness of 1.7 mm. Cheng et al. investigated the microwave absorption mechanism of hexagonal barium ferrites doped with La^{3+} ; it showed that microwave absorption was enhanced for the improved complex permittivity and permeability. The minimum reflection loss (RL) of -39.15 dB was obtained with thickness of 2.4 mm, and the bandwidth of $\text{RL} < -10$ dB can reach 11.5 GHz when the thickness is 2.0 mm [12]. However, some disadvantages like high density, low dielectric loss and narrow frequency bandwidth restrict their further applications as microwave absorbers. In order to solve the above problems, related researchers are often devoted to the recombination of barium ferrite and dielectric materials, such as conductive polymers, graphene, carbon nanotubes, and so on. Cao et al. [13] investigated $\text{Fe}_3\text{O}_4/\text{MWCNTs}$ and $\text{PANI}/\text{Fe}_3\text{O}_4/\text{MWCNTs}$ with respect to highly efficient microwave absorption and effective absorption bandwidth; the result showed that $\text{Fe}_3\text{O}_4/\text{MWCNTs}$ exhibited enhanced magnetic properties coupled with increased dielectric properties. As is well known, polyaniline has great potential in absorbing materials with lightweight, adjustable electromagnetic parameters and excellent chemical and environmental stability [6, 14]. Therefore, polyaniline is a suitable substrate material which is often compounded with ferrite to improve microwave absorption. For example, Liu et al. [15] reported the electromagnetic properties of $\text{BaFe}_{12}\text{O}_{19}/\text{PANI}$ nanocomposites with core-shell structure, the optimal reflection loss (RL) of which can reach -28 dB at 12.8 GHz with a broad effective EM wave absorption

bandwidth ($\text{RL} < -10$ dB) of 5.3 GHz and a corresponding thickness of 2 mm. Feng et al. [16] synthesized a composite of $\text{BaFe}_{12}\text{O}_{19}$ prepared in different temperature with polyaniline; the minimal RL is -17.6 dB at 17.2 GHz with the thickness of 4.5 mm.

Although the measure of combining the conducting polymer and ferrites can improve microwave absorption properties, the percolation threshold of PANI is high because of low compatibility and low aspect ratio of the conducting polymer. [17]. Graphene, a monolayer or few layers honeycomb structure composed by two-dimensional sp^2 bonded sheet, has become a popular material for electromagnetic interference shielding owing to its lightweight, high specific surface, superior mechanical strength and excellent dielectric property [12, 18, 19]. Besides, graphene has a high aspect ratio, which is propitious to formation of a conductive network, leading a lower conduction threshold. Nonetheless, single graphene shows a high reflection on the surface of absorber, which is attributed to impedance mismatch arising from its excellent dielectric loss and negligible magnetic loss. Thus, RGO is compounded with magnetic materials to balance the relationship between dielectric and magnetic losses and further improve the microwave absorption performance. As in the case of 3D flowerlike $\text{Co}_3\text{O}_4/\text{RGO}$ nanocomposites surveyed by Ma et al. [20], where the minimum RL of $\text{Co}_3\text{O}_4/\text{RGO}$ can be up to -61 dB, the bandwidth exceeding -10 dB is 4 GHz. To the best of our knowledge, there are few reports on the fabrication and microwave absorption properties of the novel ternary composites including RGO, different magnetic particles and PANI.

Inspired by the above facts, a novel ternary composite consisting of $\text{BaTb}_{0.2}\text{Eu}_{0.2}\text{Fe}_{11.6}\text{O}_{19}/\text{PANI}$ decorating reduced graphene oxide has been synthesized by three-step method and their microwave absorption properties are investigated. The results demonstrate that the M_s will increase with the Tb^{3+} and Eu^{2+} doping $\text{BaFe}_{12}\text{O}_{19}$. Meanwhile, the synergistic effect of $\text{BaTb}_{0.2}\text{Eu}_{0.2}\text{Fe}_{11.6}\text{O}_{19}/\text{PANI}/\text{RGO}$ composite can enhance microwave absorption performance. The other related mechanism of the RL for the $\text{BaTb}_{0.2}\text{Eu}_{0.2}\text{Fe}_{11.6}\text{O}_{19}/\text{PANI}/\text{RGO}$ composites will be explained in detail.

Experimental

Materials

Graphite powder (flake graphite, grade 325) was purchased from Pilot Chemical Corporation (Shanghai, China). Other chemical reagents and solvents were purchased from the Sinopharm Chemical Reagent Co., Ltd., China. All the chemicals were used as-received without further purification.

Preparation of $\text{BaTb}_{0.2}\text{Eu}_{0.2}\text{Fe}_{11.6}\text{O}_{19}$ nanoparticles

Sample with composition of $\text{BaTb}_{0.2}\text{Eu}_{0.2}\text{Fe}_{11.6}\text{O}_{19}$ (BTEFO) nanoparticles is prepared by the chemical co-precipitation method. Firstly, nitrates of Ba, Fe, Tb and Eu in stoichiometric proportion are dissolved in 100 mL deionized water and stirred for 30 min to form a homogeneous solution of metal salt solution. Next, appropriate NaOH solution (1 mol/L) is added to the above solution drop by drop until the pH of solution is 10. Meanwhile, the solution is continuously mechanical stirred for 6 h. Then, the mixture is filtered to obtain the precipitated products, which are washed with deionized water and ethyl alcohol for several times. Followed by that, the sample is dried at 60 °C in oven for 24 h to acquire the precursor, which is sintered at 950 °C for 2 h with a heating rate of 5 °C/min to obtain the BTEFO nanoparticles.

Synthesis of binary BTEFO/PANI nanocomposites

The BTEFO/PANI composite is synthesized via an in situ polymerization method. The typical process is described as follows: Initially, 1.0 g BTEFO nanoparticles and 2.0 mL aniline monomer are added to 200 mL solution that containing 0.1 mol/L hydrochloric acid (HCl). Then, the mixture is dispersed by ultrasonic for 30 min at the temperature no more than 5 °C. Meanwhile, 2.5 g ammonium persulfate (APS) is dissolved in 20 mL HCl solution. After that, the APS solution is added to the above mixture solution dropwise with vigorous stirring for 12 h. Finally, the product is washed with distilled water and absolute ethyl alcohol several times and dried in vacuum oven at 60 °C for 24 h.

Fabrication of ternary BTEFO/PANI/RGO nanocomposites

Graphene oxide (GO) is prepared from purified natural graphite by using modified Hummers method as reported elsewhere [21]. In a typical step, a certain quantity of GO and the prepared BTEFO/PANI composite powders are dissolved in 60 mL of deionized water with sonication for 2 h to form a homogeneous dispersion. Then, moderate hydrazine hydrate is added to the mixture with constant stirring at 95 °C for 12 h. The mass ratio of hydrazine hydrate and GO is 0.7. Finally, the product is filtered, washed with distilled water and absolute ethyl alcohol to remove impurities and dried in vacuum oven at 60 °C for about 24 h. Besides, we also fabricate different weight ratios of BTEFO/PANI and RGO (20:1, 20:2, 20:3 and 20:4), which are denoted as C-1, C-2, C-3 and C-4, respectively. This synthetic process is summarized in Fig. 1.

Characterization

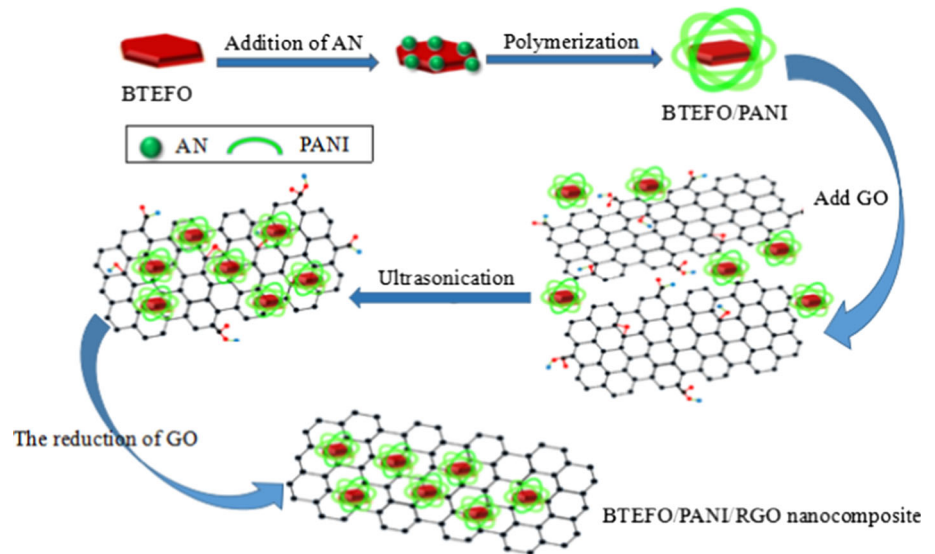
The resulting powder is characterized by X-ray powder diffraction (XRD) using a diffractometer (RIGAKU, model D/max) with $\text{CuK}\alpha$ radiation of wavelength $\lambda = 1.5418 \text{ \AA}$. Its morphology is studied with a transmission electron microscope (JEOL, model JEM 2001). Raman spectra are measured using a laser Raman spectrometer (Thermo Fisher, model DXR) at a 663 nm wavelength incident laser light. Magnetization measurements are taken at room temperature (293 K) using a vibrating sample magnetometer (LDJ, model 9600-1). Meanwhile, the electromagnetic parameters are analyzed by a network analyzer (Agilent Technologies, model E8363B), in which the powders are mixed with 50 wt% paraffin, and the samples are pressed into toroidal shape with the outer diameter of 7 mm, inner diameter of 3 mm and thickness of 2 mm.

Results and discussion

Morphological and structural characterization

The XRD patterns of RGO, BTEFO, BTEFO/PANI nanocomposites and BTEFO/PANI/RGO nanocomposites are shown in Fig. 2. The two characteristic

Figure 1 Schematic representation of the preparation of the BTEFO/PANI/RGO nanocomposites.



diffraction peaks at $2\theta = 20.47^\circ$ and 25.13° are assigned to (100) and (110) planes of PANI in Fig. 2e [22]. It can be observed from Fig. 2a that RGO exhibits two broad peaks at $2\theta = 24.15^\circ$ and 43.45° , corresponding to the (002) and (001) planes [12]. As can be seen from Fig. 2b, there are several sharp diffraction peaks centered at 30.2° , 32.2° , 34.1° , 37.2° , 40.4° and 42.5° , which can be well indexed to the (100), (008), (107), (114), (200) and (201) crystal planes of M-type hexaferrite barium ferrite [2] and no second phase can be found, manifesting that the Tb^{3+} and Eu^{2+} can enter the lattice and do not affect the crystal structure of hexagonal barium ferrite. We can find

that the peaks of the BTEFO and PANI still exist in Fig. 2c, indicating that BTEFO/PANI nanocomposites are successfully prepared. However, the diffraction peaks of BTEFO in BTEFO/PANI nanocomposites show a slight displacement compared with that of standard diffraction peaks. The diffraction peaks of BTEFO/PANI/RGO nanocomposites are shown in Fig. 2d; the characteristic peaks of RGO cannot be observed. This may be attributed to its low diffraction intensity and content in the BTEFO/PANI/RGO nanocomposites. The similar phenomenon also was reported in the previous literature [23].

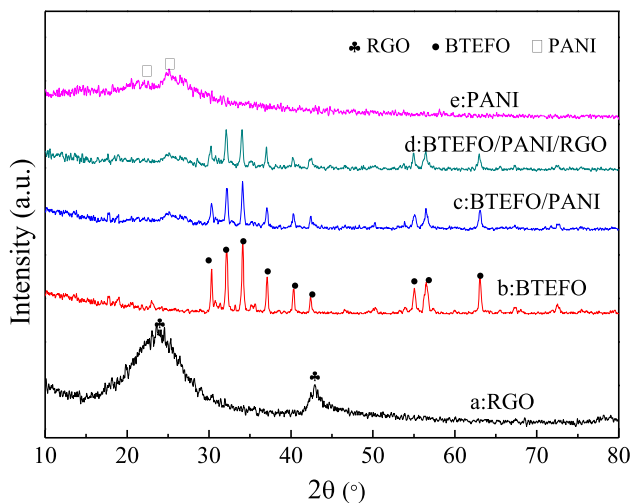


Figure 2 XRD patterns of (a) RGO, (b) BTEFO, (c) BTEFO/PANI nanocomposite, (d) BTEFO/PANI/RGO nanocomposite and (e) PANI.

The FTIR spectra of BTEFO/PANI and BTEFO/PANI/RGO nanocomposites are exhibited in Fig. 3. The characteristic peaks that derive from Fe–O and Ba–O bond stretching vibration at 435 cm^{-1} , 513 cm^{-1} and 602 cm^{-1} are observed from the FTIR spectrum of BTEFO/PANI, which represents the form of BTEFO particles in the composites [24]. Moreover, it also can be clearly observed the absorption peak of PANI from Fig. 3a. The peak at 807 cm^{-1} is corresponding to the C–H of the benzenoid unit. There is a peak appearing at 1142 cm^{-1} , which is closely relevant to the aromatic C–H inplane bending mode. The peaks at 1249 cm^{-1} and 1298 cm^{-1} are associated with the asymmetric C–N stretching mode for benzenoid ring. The C=N stretching and C=C stretching of the quinoid and benzenoid rings on PANI molecular chain are observed, which correspond to two peaks at 1496 cm^{-1} and 1574 cm^{-1} , respectively. The

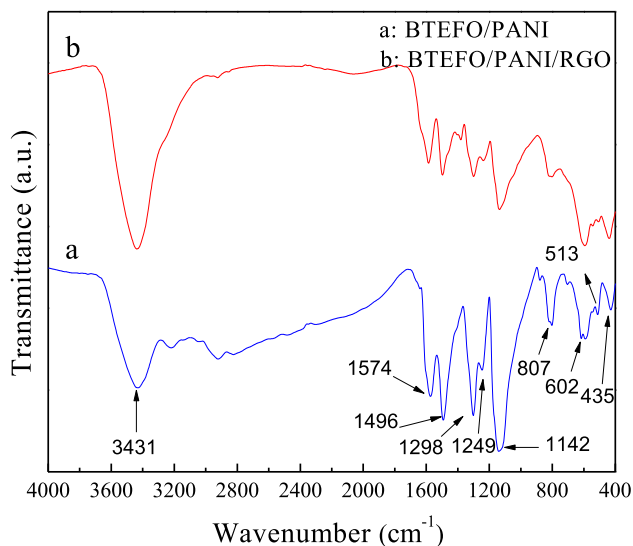


Figure 3 FTIR spectra of (a) BTEFO/PANI nanocomposites, (b) BTEFO/PANI/RGO nanocomposites.

relatively broad peak arises at about 3431 cm^{-1} owing to the stretching vibration and deformation vibration of hydroxyl group acquired from wet atmosphere [25, 26]. The relative peaks of BTEFO/PANI also are found in Fig. 3b. However, we cannot find the peak of oxygen-containing functional groups on the GO, which indicates that GO is completely reduced by hydrazine hydrate [17].

To further investigate the morphology and structure of the samples, the TEM images for the BTEFO/PANI and BTEFO/PANI/RGO nanocomposites are presented in Fig. 4. Figure 4a, b reveals the low- and high-magnification TEM images of BTEFO/PANI nanocomposites. It can be clearly seen that the average size of the BTEFO nanoparticles uniformly coated by PANI molecular chains in the range of 50–100 nm and the microstructure of BTEFO nanoparticles is polygonal. The HRTEM images in Fig. 4c, d show the fringe spacing values that are measured to be 0.286 nm, 0.304 nm and 0.265 nm, corresponding to the (112), (106) and (104) crystal planes of BTEFO nanoparticles, severally. The TEM image of the BTEFO/PANI/RGO nanocomposites is displayed in Fig. 4e. It is observed that the RGO is diaphanous with some wrinkles. Furthermore, the nanosheet of RGO is firmly anchored on the surface of the BTEFO/PANI nanocomposites.

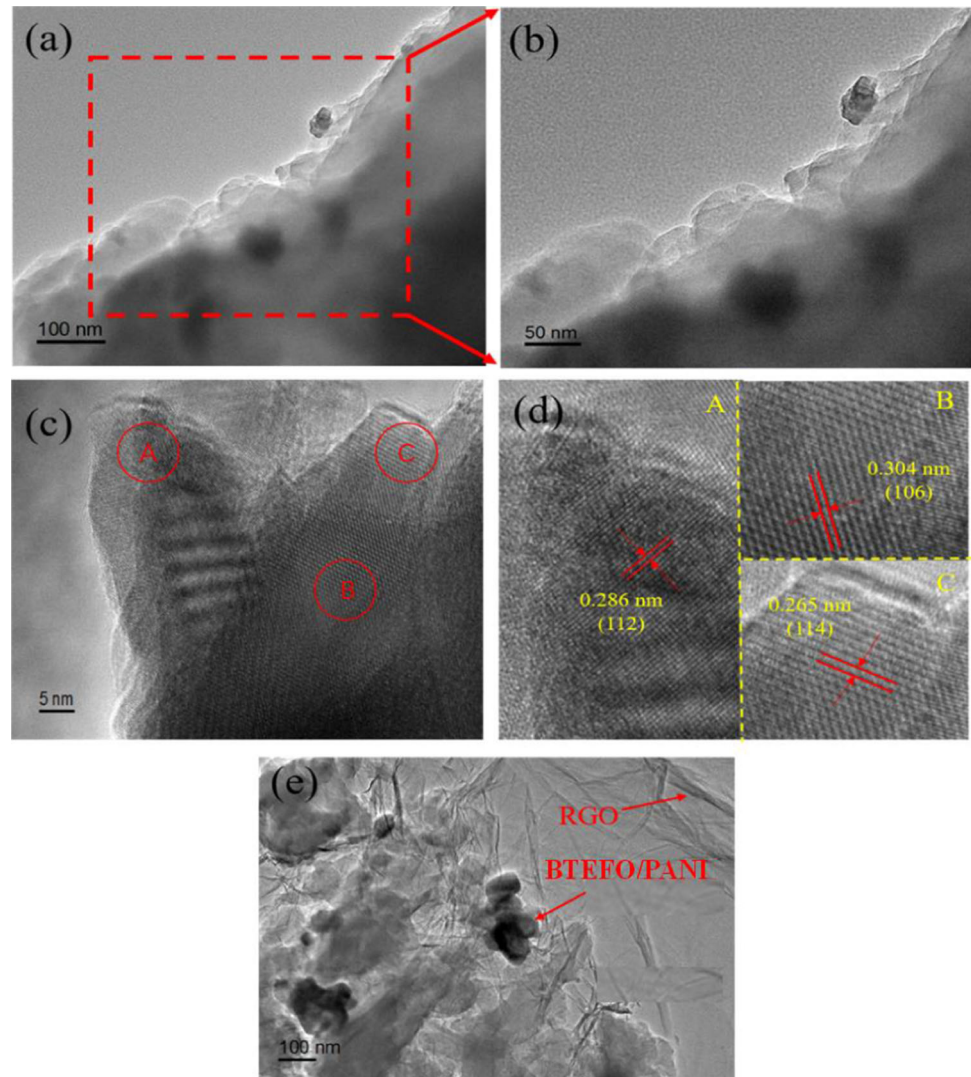
To explore the structural change of graphene and graphene-based composites, the Raman spectroscopy of the various samples is exhibited in Fig. 5. For the

GO in Fig. 5a, the two peaks called D band and G band appear at 1331 cm^{-1} and 1586 cm^{-1} , which are attributed to the breathing mode of k-point phonons of A_{1g} and the tangential stretching mode of the E_{2g} phonons of sp^2 atoms, respectively [11]. It is observed that the peaks at 1161 cm^{-1} , 1402 cm^{-1} and 1484 cm^{-1} are associated with C–H stretching vibration of the quinoid/phenyl group, the C–N stretching vibration of benzenoid ring and the semiquinone radical cation structure of PANI in Fig. 5b, respectively, which manifests the existence of PANI in the BTEFO/PANI nanocomposites [27]. The characteristic peaks of the RGO and PANI can be found from the Raman spectrum curve of the BTEFO/PANI/RGO nanocomposites, whereas the peaks of PANI and RGO in ternary nanocomposites show slightly shift compared with that of PANI in binary nanocomposites and GO. This phenomenon implies the presence of charge transfer among BTEFO, PANI and RGO [28].

Magnetic property analysis

The field dependence of magnetization is measured with VSM at room temperature. The obtained hysteresis loops and related magnetic parameters (the saturation magnetization (M_s) and coercivity (H_c)) are shown in Fig. 6. As can be seen from Fig. 6a, the M_s of BTEFO is higher than that of pure $\text{BaFe}_{12}\text{O}_{19}$, but the H_c value of BTEFO is decreased compared with that of pure $\text{BaFe}_{12}\text{O}_{19}$. The increase in M_s and the decrease in H_c can be attributed to ion occupancy and the difference in ionic magnetic moments. Fe^{3+} ions are distributed over five sites in barium ferrites, namely 12k, 2a, 2b, $4f_1$ and $4f_2$, with three spin-up positions (12k, 2a and 2b) and two spin-down positions ($4f_1$ and $4f_2$). When Fe^{3+} ions (magnetic moment = $5\ \mu\text{B}$) are substituted by magnetic ions Tb^{3+} ($7.5\ \mu\text{B}$) and Eu^{2+} ($7\ \mu\text{B}$), the total magnetic moment will increase and further enhance the M_s . H_c declines with the Tb^{3+} and Eu^{2+} doping, which may ascribe the decrease in the anisotropy field (H_a). The substitution may change the anisotropy field, H_a , expressed by the relation: $H_a = 2K_1/M_s$, where K_1 is the first anisotropy constant and M_s is the saturation magnetization [29]. H_c of a magnetic material is proportional to H_a . Relevant research shows that different sites of Fe^{3+} ions contribute differently to K_1 . Xu et al. [30] once calculated the K_1 value about 2a, 2b, $4f_1$, $4f_2$ and 12k sites; the result shows that the

Figure 4 TEM images (a, b) and HRTEM images (c, d) of BTEFO/PANI, TEM image (e) of BTEFO/PANI/RGO nanocomposites.



values of K_1 are 0.23, 1.40, 0.18, 0.51 and -0.18 , respectively. In this study, Tb^{3+} prefers to occupy the tetrahedral $4f_1$ sublattice, while Eu^{2+} ions tend to locate in an octahedral $2a$ position; the sublattices of $4f_1$ and $2a$ have little influence on K_1 which can be neglected. Thus, H_c diminishes with M_s increasing [11]. In the next place, we research the dependence of M_s and H_c on RGO content. As can be observed from Fig. 6b and c, the M_s and H_c values of the nanocomposites decrease gradually from 13.87 emu/g and 6209 Oe to 12.66 emu/g and 5283 Oe, respectively. It is evident that the M_s and H_c of the ternary composites decrease gradually with the increasing content of RGO since RGO is non-magnetic material.

Microwave absorption properties analysis

The real permittivity (ϵ') and imaginary permittivity (ϵ'') of four samples in the range of 2–18 GHz are shown in Fig. 7. As can be observed from Fig. 7a, b, with the increasing content of RGO, the ϵ' and ϵ'' of the composites also increase gradually from 4.5 to 10.5 and 1.3 to 9.0, respectively. This phenomenon can be explained as the following reasons: Firstly, RGO is a dielectric material with a higher conductivity, which will exert an effect on the real permittivity. Secondly, there is a charge transfer among BTEFO, PANI and RGO, which may cause the electronic polarization. Thirdly, the increased dipole polarization caused by defects and abundant surface functional groups in RGO plays a very important role

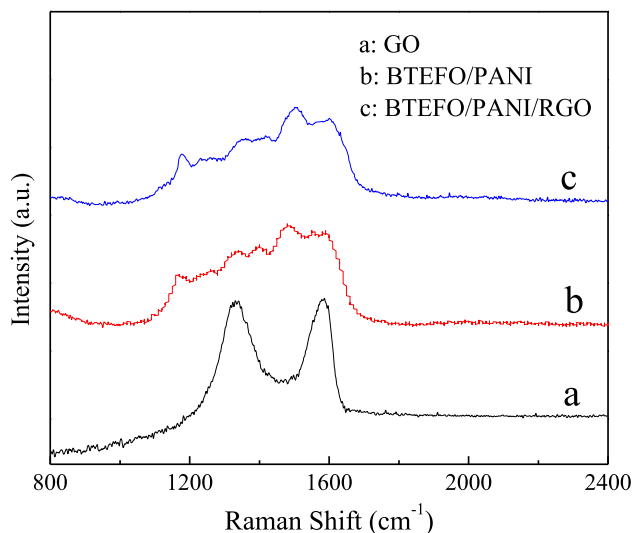


Figure 5 Raman spectra of (a) GO, (b) BTEFO/PANI nanocomposite, and (c) BTEFO/PANI/RGO nanoparticles.

in the imaginary permittivity [31]. Finally, with the addition of graphene, the interface of ternary composites will increase and that can induce interfacial polarization at microwave frequency [32]. Meanwhile, it is obviously found the downward trend of the ϵ' and ϵ'' values with increasing frequency from 2 to 18 GHz, which is ascribed to the following fact. In the frequency range of 2–18 GHz, the polarization of molecules and electrons cannot have enough time to catch up with the change in applied alternating electromagnetic field [33].

Figure 8 displays the real permeability (μ') and imaginary permeability (μ'') of BTEFO/PANI/RGO nanocomposites in the frequency range of 2–18 GHz. As noted in Fig. 8, the variable trends of four samples have little difference. The values of μ' are in the range of 1.02–1.19, 0.98–1.15, 1.01–1.16 and 1.01–1.12, respectively, indicating a slight fluctuation. Meanwhile, with the frequency increasing from 2 to 18 GHz, a slight decline occurs for the μ'' . In addition, there are three resonance peaks in μ'' at ~ 4.88 GHz, ~ 12 GHz and ~ 15.12 GHz, respectively.

In this paper, the BTEFO nanoparticles make a great contribution to magnetic loss of the ternary nanocomposites, which derive from hysteresis loss, domain wall resonance, eddy current effect and natural resonance [34]. In general, the hysteresis loss is negligible in a weak applied field and the domain wall resonance usually occurs in the frequency range

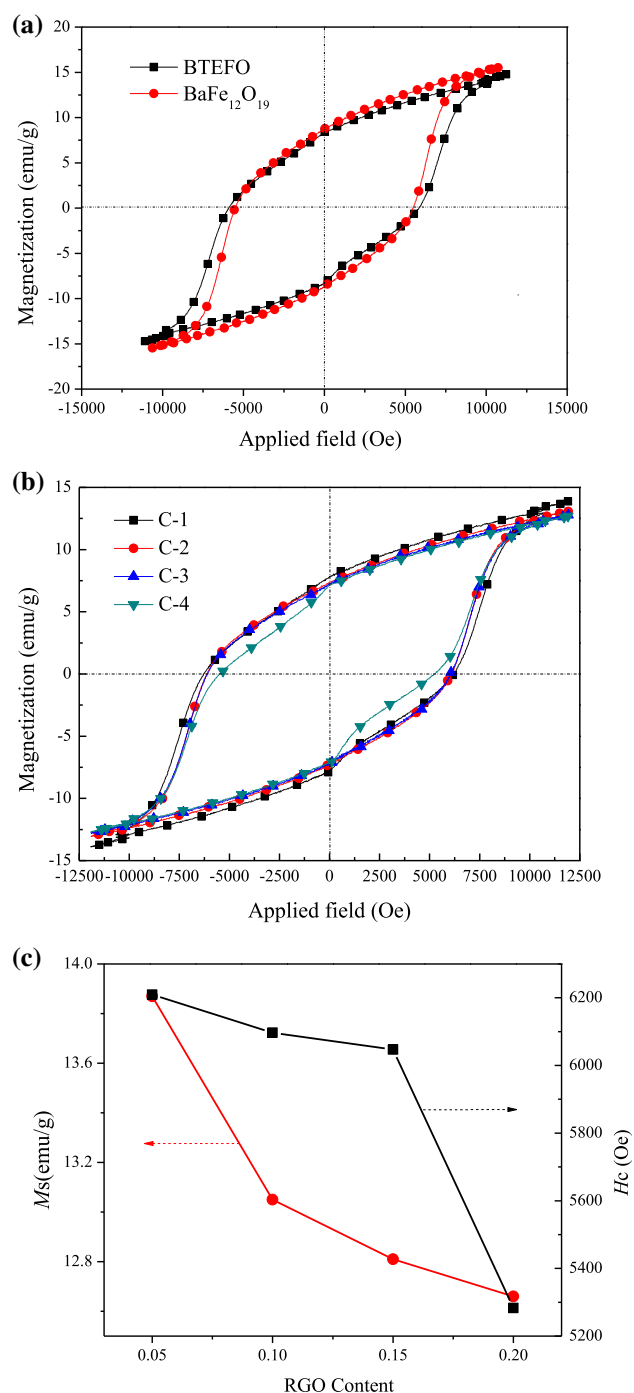
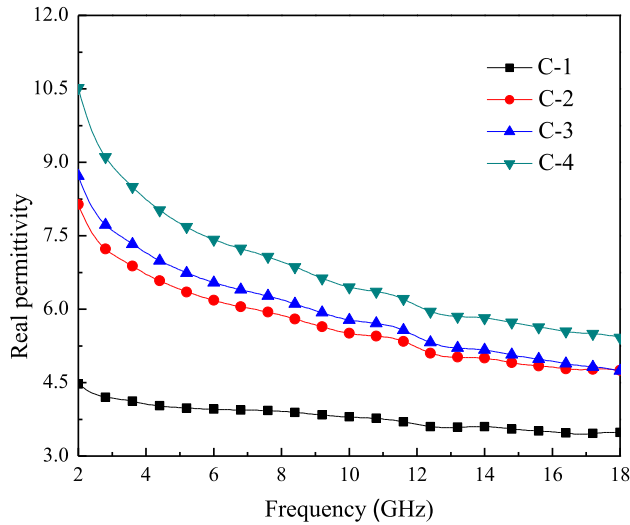
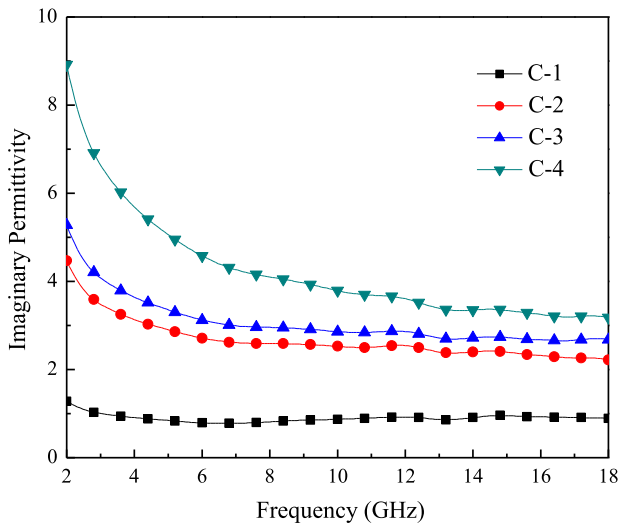


Figure 6 Magnetization hysteresis loops of **a** $\text{BaFe}_{12}\text{O}_{19}$ and BTEFO nanoparticles, **b** BTEFO/PANI/RGO nanocomposite with different addition of RGO, and **c** saturation magnetization M_s and coercivity H_c of BTEFO/PANI/RGO samples.

of MHz. Therefore, the magnetic loss depends on eddy current effect and natural resonance in this study. The eddy current loss can be evaluated by [15]



(a)



(b)

Figure 7 Real permittivity (a) and imaginary permittivity (b) of BTEFO/PANI/RGO nanocomposites.

$$\mu'' \approx \frac{2\pi\mu_0(\mu')^2\sigma d^2 f}{3} \tag{1}$$

where σ and μ_0 are the electric conductivity and the permeability in vacuum, respectively. Thus, C_0 can be described by

$$C_0 = \mu''(\mu')^{-2}f^{-1} = \frac{2\pi\mu_0\sigma d^2}{3} \tag{2}$$

When the frequency is varied, the values of C_0 keep constant, implying that the magnetic loss results from eddy current loss. The C_0 - f curves of the four samples are exhibited in Fig. 9. It is clearly observed that the

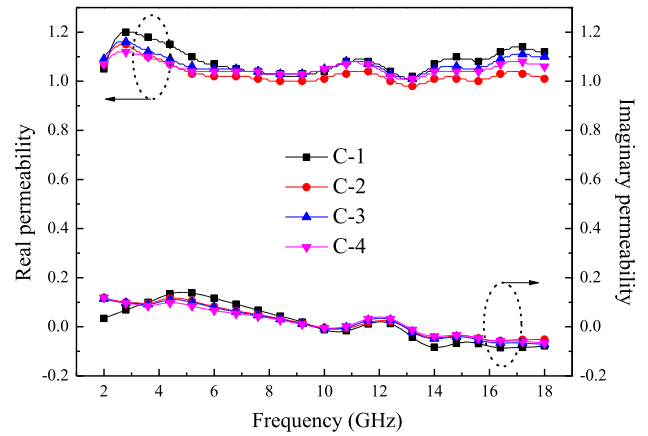


Figure 8 Real parts and imaginary parts of the complex permeability of BTEFO/PANI/RGO nanocomposites.

C_0 values drastically decrease in the range from 2 to 16 GHz, whereas C_0 keeps approximately constant when $f > 16$ GHz. As a result, we believe that the magnetic loss of the samples at ~ 4.88 GHz, ~ 12 GHz and ~ 15.12 GHz shown in Fig. 9 can be caused by natural resonance.

Moreover, some reports manifested that the enhancement of microwave absorption is related to Debye dipolar relaxations. According to the Debye theory, the relative complex permittivity can be expressed by the following equations [3, 35]:

$$\epsilon_r = \epsilon_\infty + \frac{\epsilon_s - \epsilon_\infty}{1 + j2\pi f\tau} = \epsilon' - j\epsilon'' \tag{3}$$

where f , ϵ_s , ϵ_∞ and τ are frequency, static permittivity, relative dielectric permittivity at the high-frequency limit, and polarization relaxation time, respectively. Thus, ϵ' and ϵ'' can be described by

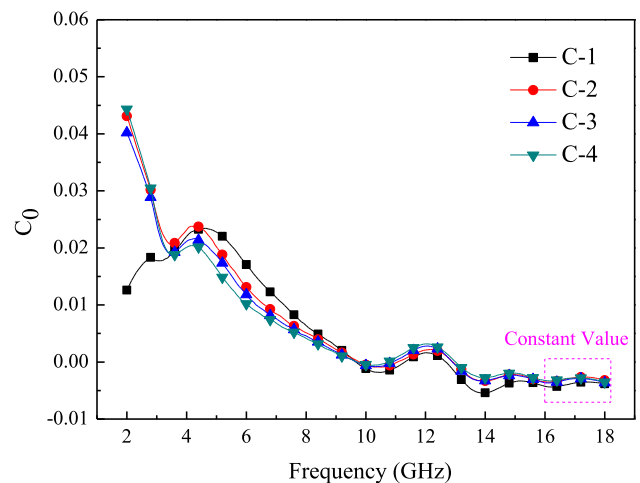


Figure 9 $C_0 - f$ values of BTEFO/PANI/RGO nanocomposites.

$$\varepsilon' = \varepsilon_{\infty} + \frac{\varepsilon_s - \varepsilon_{\infty}}{1 + (2\pi f)^2 \tau^2} \quad (4)$$

$$\varepsilon'' = \frac{2\pi f \tau (\varepsilon_s - \varepsilon_{\infty})}{1 + (2\pi f)^2 \tau^2} \quad (5)$$

Based on Eqs. (2) and (3), the relationship between ε' and ε'' can be deduced as follows:

$$\left(\varepsilon' - \frac{\varepsilon_s + \varepsilon_{\infty}}{2}\right)^2 + (\varepsilon'')^2 = \left(\frac{\varepsilon_s - \varepsilon_{\infty}}{2}\right)^2 \quad (6)$$

Thus, the curve of ε' versus ε'' is a single semicircle, which is generally called the Cole–Cole semicircle. Each semicircle corresponds to one Debye relaxation process. The curves of ε' versus ε'' of the four samples are displayed in Fig. 10. It is clearly seen that the C-1 and C-2 both present three Cole–Cole semicircles, and the Cole–Cole semicircles of C-3 and C-4 are one more than that of C-1 and C-2. It illustrates that there are multiple relaxation for four samples, which is in favor of microwave absorption. Meanwhile, relatively speaking, the EM wave can be more effectively

attenuated by the C-3 and C-4 samples. The relaxation process with respect to a changing electric field in a dielectric medium arises from the interface polarizations of BTEFO/PANI, BTEFO/RGO and PANI/RGO.

To clarify the microwave properties of the as-prepared samples, the reflection loss (RL) curves can be calculated according to the transmission line theory, which is on basis of the relative complex permeability and permittivity mentioned above with a given frequency range and a given absorber thickness (d) by the following equations [36, 37]:

$$RL = 20 \log \left| \frac{Z_{in} - Z_0}{Z_{in} + Z_0} \right| \quad (7)$$

in which Z_0 is the impedance of free space and Z_{in} is the input impedance of the absorber expressed as

$$Z_{in} = Z_0 \left(\frac{\mu_r}{\varepsilon_r} \right)^{\frac{1}{2}} \tanh \left\{ j \left(\frac{2\pi f d}{c} \right) (\mu_r \varepsilon_r)^{\frac{1}{2}} \right\} \quad (8)$$

where μ_r and ε_r are the relative complex permeability and permittivity, f is the frequency of electromagnetic

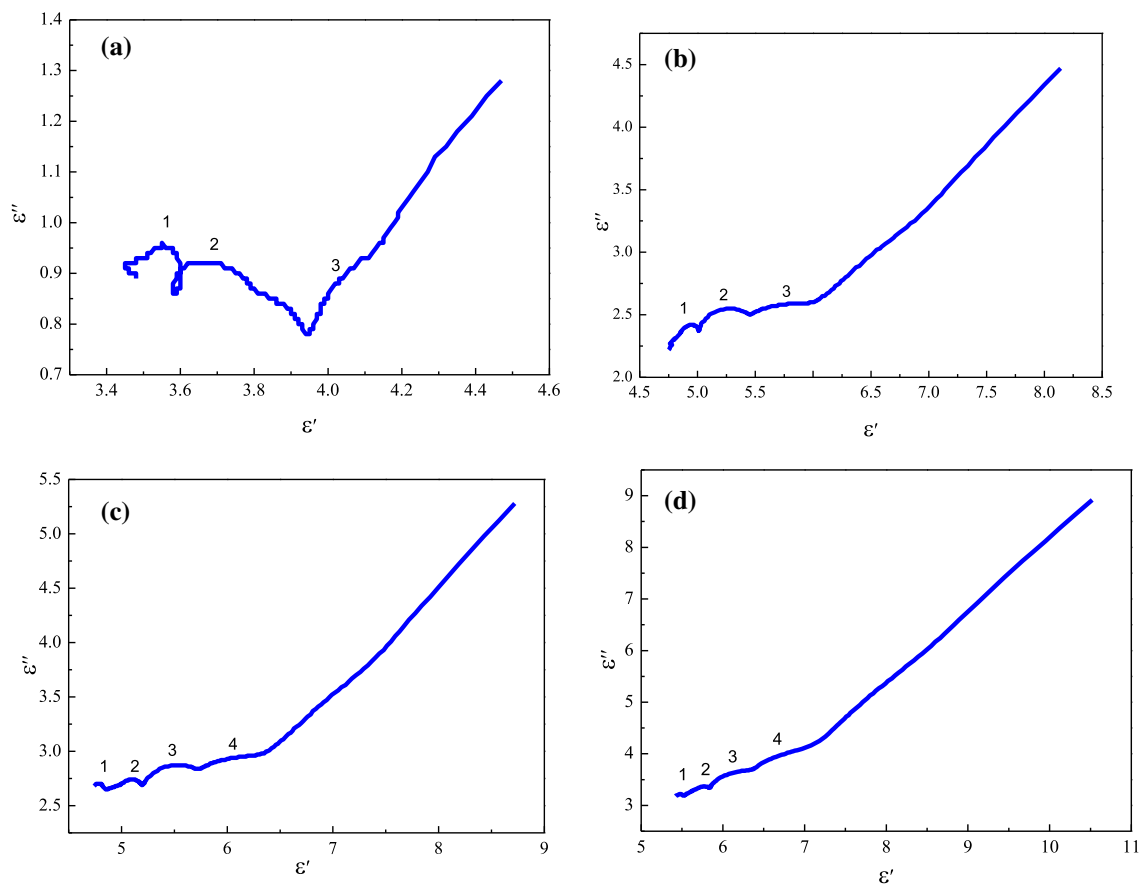


Figure 10 Cole–Cole plots of BTEFO/PANI/RGO composites with different RGO addition in 2–18 GHz.

wave, d is the thickness of the absorber, and c is the velocity of light in vacuum. Figure 11 illustrates the 3D RL plots of BTEFO/PANI/RGO samples versus frequency and thickness with different RGO content. In Fig. 11a, we can observe that the minimum RL value is only -8.3 dB, which shows a poor microwave absorption ability. However, with increase in the RGO proportions, the microwave absorption performances of composite are significantly enhanced. For C-2 nanocomposites, exhibited in Fig. 11b, the minimum RL value is -32.5 dB at the frequency about 8.1 GHz, the corresponding thickness is 3.95 mm, and the bandwidth of RL below -10 dB (90% absorption) is 3.4 GHz. Figure 11c presents the minimum RL value of C-3 which is -51.1 dB at the frequency about 8.8 GHz with

3.55 mm matching thickness and the effective bandwidth is 3.6 GHz. As can be seen from Fig. 11d, an optimal RL value of -60.9 dB at 16.4 GHz with a thickness of only 1.95 mm and a broad effective bandwidth of 4.2 GHz are achieved for the C-4 composites. In addition, it is worth noting that the minimum reflection loss peaks shift to lower frequency with an increasing thickness. This phenomenon can be ascribed to quarter-wavelength attenuation, which is caused by the inverse phase angle of the reflection microwave from the upper and bottom surface of absorber [37].

In order to explain the mechanism of EM absorption, the dielectric loss tangents ($\tan \delta_E = \epsilon''/\epsilon'$) and the magnetic loss tangents ($\tan \delta_M = \mu''/\mu'$) of the C-1, C-2, C-3 and C-4 are presented in Fig. 12a–d,

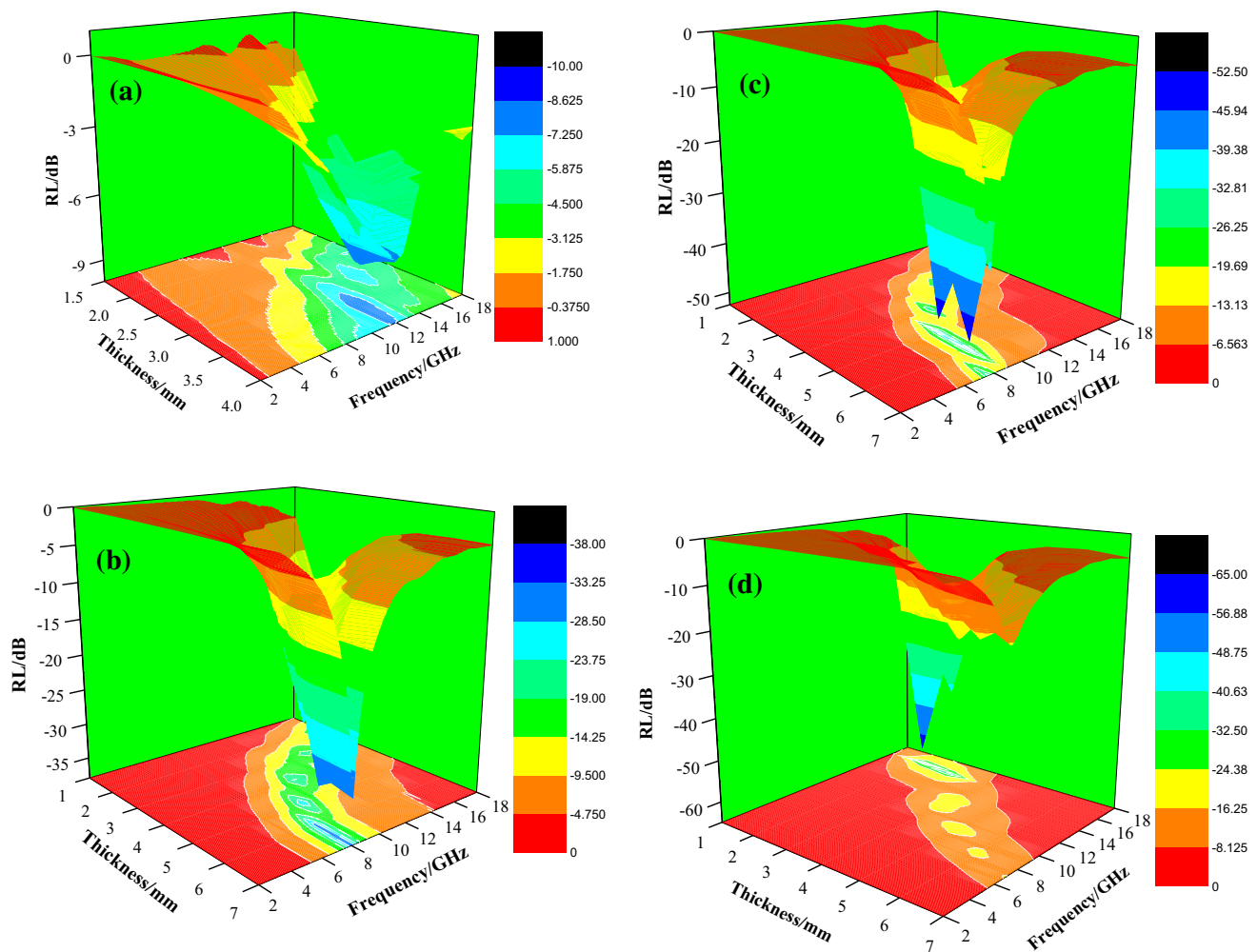


Figure 11 3D plots of the calculated reflection loss of samples loaded with different concentrations of BTEFO/PANI/RGO composites (a–d) versus frequency and thickness.

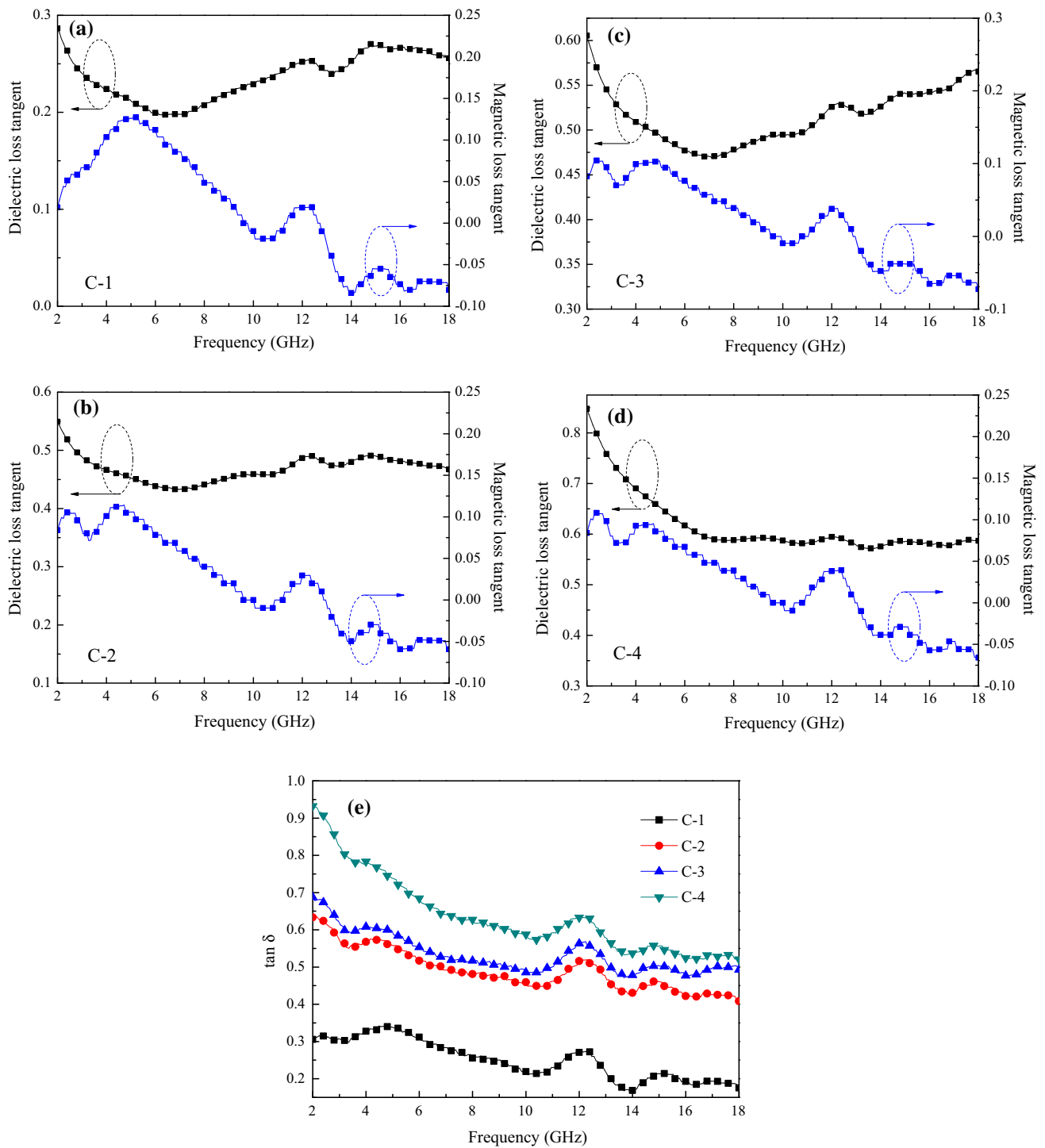


Figure 12 Tangent loss of BTEFO/PANI/RGO nanocomposites.

respectively. It reveals that the values of $\tan \delta_E$ are significantly larger than those of $\tan \delta_M$, indicating that the electromagnetic wave attenuation mechanism of which mainly depends on the dielectric loss.

Furthermore, we also calculate the loss tangents ($\tan \delta = \tan \delta_E + \tan \delta_M$) of the samples, as shown in Fig. 12e. The $\tan \delta$ values of the BTEFO/PANI/RGO show an increasing trend with the addition of RGO

content. The loss tangents of the C-4 are the highest among the four samples, the microwave absorption of which may be the best.

Meanwhile, the attenuation constant α also plays a major role in enhancing microwave absorption properties. The α can be defined as [14]

$$\alpha = \frac{\sqrt{2\pi f}}{c} \times \sqrt{(\mu''\epsilon'' - \mu'\epsilon') + \sqrt{(\mu''\epsilon'' - \mu'\epsilon')^2 + (\mu'\epsilon'' + \mu''\epsilon')^2}} \tag{9}$$

where f is the frequency of electromagnetic wave propagation and c is the velocity of light. It is found from Fig. 13 that the four samples display a similar variation with the increasing mass fraction of RGO.

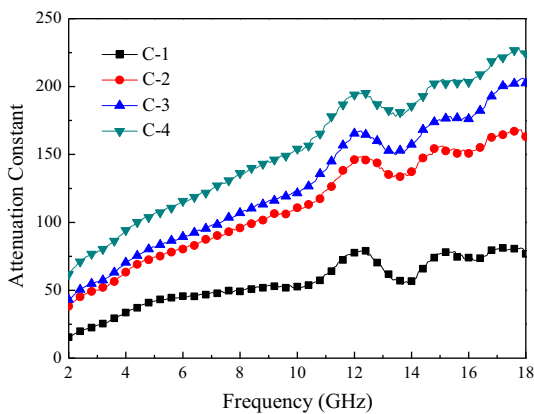
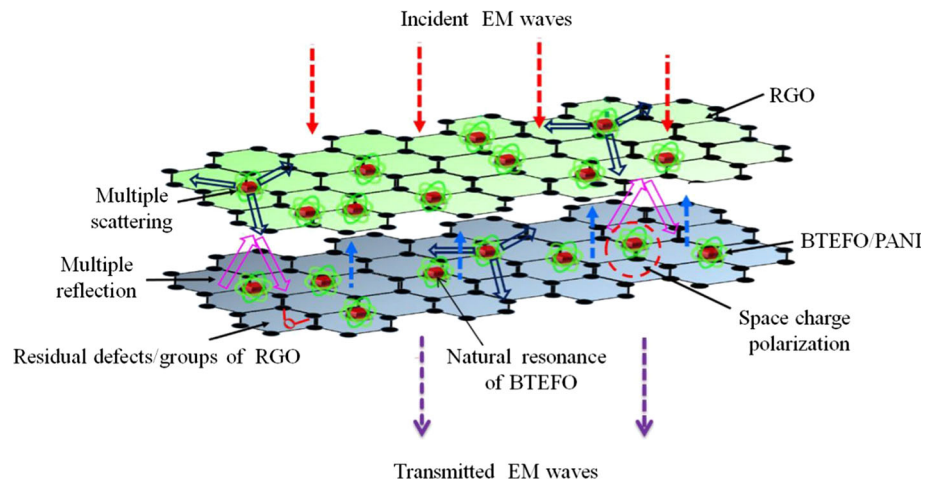


Figure 13 Microwave attenuation constants (α) of BTEFO/PANI/RGO nanocomposites.

Figure 14 Schematic representation of the microwave attenuation mechanism in BTEFO/PANI/RGO nanocomposites.



C-4 has the highest α , indicating that the microwave attenuation is the best.

According to the above analysis, we confirm that the BTEFO/PANI/RGO nanocomposites possess remarkable absorbing properties. The microwave absorption mechanism is shown in Fig. 14. Firstly, the proper combination of the complex permittivity and permeability results in the appropriate synergistic effect of dielectric loss and magnetic loss [38]. Secondly, the special structure of the composite is fundamental to the enhancement of the absorption property. The hexagonal BTEFO, fibrous PANI and the relatively large surface area of RGO can provide more active sites for multiple reflections and scattering, transforming the microwave energy to heat energy in long propagation periods [39]. Moreover, there are many interfaces among BTEFO nanoparticles, PANI and RGO sheets, resulting in interfacial polarization and associated relaxation, which generate a positive effect on electromagnetic wave absorption [40]. Thirdly, the increased dipole polarization caused by defects and abundant surface functional groups in RGO enhance the dielectric loss [41, 42]. Fourthly, there will be a charge transfer among BTEFO nanoparticles, PANI and RGO (can be observed in the Raman spectroscopy), and Tb^{3+} , Eu^{2+} doping $BaFe_{12}O_{19}$ induce lattice distortion; the free charge will accumulate and cause space charge polarization [27, 32, 43]. Finally, BTEFO will generate natural resonance because of its nanoscale which contributes to magnetic loss [40].

Conclusions

All in all, the simple fabrication of magnetic and conductive BTEFO/PANI/RGO hybrids with different component proportion has been demonstrated. BTEFO/PANI/RGO nanocomposites exhibit an excellent microwave absorption performance since its preeminent impedance matching and attenuation matching. For C-4, superior reflection loss of -60.9 dB is achieved at 16.4 GHz with a thickness of only 1.95 mm and the absorption bandwidths exceeding -10 dB are 4.2 GHz. Therefore, it is believed that the BTEFO/PANI/RGO nanocomposites can be an outstanding microwave absorber with thin thickness, lightweight, wide frequency band and strong microwave absorption performance.

Acknowledgements

This work was supported by the Flagship Major Development of Jiangsu Higher Education Institutions (Grant No. PPZY2015A025) and Jiangsu Provincial Department of Education (Grant No. 18KJA430016) and Joint Open Fund of Jiangsu Collaborative Innovation Center for Ecological Building Material and Environmental Protection Equipments and Key Laboratory for Advanced Technology in Environmental Protection of Jiangsu Province and Key Laboratory for Ecological-Environment Materials of Jiangsu Province (Grant No. JH201826).

References

- [1] Ding D, Wang Y, Li XD, Qiang R, Xu P, Chu WL, Han XJ, Du YC (2017) Rational design of core-shell Co@C microspheres for high-performance microwave absorption. *Carbon* 111:722–732
- [2] Verma M, Singh AP, Sambyal P, Singh BP, Dhawan SK, Choudhary V (2015) Barium ferrite decorated reduced graphene oxide composite for effective electromagnetic interference shielding. *Phys Chem Chem Phys* 17:1610–1618
- [3] Liu PJ, Ng VMH, Yao ZJ, Zhou JT, Lei YM, Yang ZH, Kong LB (2017) Microwave absorption properties of double-layer absorbers based on $\text{Co}_{0.2}\text{Ni}_{0.4}\text{Zn}_{0.4}\text{Fe}_2\text{O}_4$ ferrite and reduced graphene oxide composites. *J Alloys Compd* 701:841–849
- [4] Xu HB, Bie SW, Xu YS, Yuan W, Chen Q, Jiang JJ (2016) Broad bandwidth of thin composite radar absorbing structures embedded with frequency selective surfaces. *Compos Part A Appl Sci Manuf* 80:111–117
- [5] Kim ST, Kim SS (2016) Microwave absorbance of Ni-Fe thin films on hollow ceramic microspheres dispersed in a rubber matrix. *J Alloys Compd* 687:22–27
- [6] Wang Y, Huang Y, Wang QF (2012) Preparation and magnetic properties of $\text{BaFe}_{12}\text{O}_{19}/\text{Ni}_{0.8}\text{Zn}_{0.2}\text{Fe}_2\text{O}_4$ composite ferrite. *J Magn Magn Mater* 324:3024–3028
- [7] Li YQ, Huang Y, Qi SH, Niu FF, Niu L (2011) Preparation, and magnetic and electromagnetic properties of La-doped strontium ferrite films. *J Magn Magn Mater* 323:2224–2232
- [8] Sun C, Sun KN, Chui PF (2012) Microwave absorption properties of Ce-substituted M-type barium ferrite. *J Magn Magn Mater* 324:802–805
- [9] Zhang ZY, Liu XX, Wang XJ, Wu YP, Li R (2012) Effect of Nd-Co substitution on magnetic and microwave absorption properties of $\text{SrFe}_{12}\text{O}_{19}$ hexaferrites. *J Alloys Compd* 525:114–119
- [10] Xie Y, Hong XW, Gao YH, Li MJ, Liu JM, Wang J, Lu J (2012) Synthesis and characterization of La/Nd-doped barium-ferrite/polypyrrole nanocomposites. *Synth Metals* 162:677–681
- [11] Li J, He S, Shi KZ, Wu Y, Bai H, Hong Y, Wu WJ, Meng QX, Jia DC, Zhou ZX (2018) Coexistence of broad-bandwidth and strong microwave absorption in $\text{Co}^{2+}\text{-Zr}^{4+}$ codoped barium ferrite ceramics. *Ceram Int* 44:6953–6958
- [12] Cheng YK, Ren XH (2016) Enhanced microwave absorbing properties of La^{3+} substituting barium hexaferrite. *J Supercond Nov Magn* 29:803–808
- [13] Cao MS, Yang J, Song WL, Zhang DQ, Wen B, Jin HB, Hou ZL, Yuan J (2012) Ferroferric oxide/multiwalled carbon nanotube vs polyaniline/ferroferric oxide/multiwalled carbon nanotube multihetero-structures for highly effective microwave absorption. *ACS Appl Mater Interfaces* 4:6948–6955
- [14] Singh K, Ohlan A, Pham VH, Varshney BRS, Jang J, Hur SH, Choi WM, Kumar M, Dhawan SK, Kong BS, Chung JS (2013) Nanostructured graphene/ Fe_3O_4 incorporated polyaniline as a high performance shield against electromagnetic pollution. *Nanoscale* 5:2411–2420
- [15] Liu JL, Zhang J, Li YQ, Zhang M (2015) Microwave absorbing properties of barium hexa-ferrite/polyaniline core-shell nanocomposites with controlled shell thickness. *Mater Chem Phys* 163:470–477
- [16] Feng WJ, Zhao X, Zheng WQ, Gang JT, Cao Y, Yang H (2017) Microwave absorption properties of $\text{BaFe}_{12}\text{O}_{19}$ prepared in different temperature with polyaniline nanocomposites. *Adv Mater Res* 1142:211–215
- [17] Luo JH, Shen P, Yao W, Jiang CF, Xu JG (2016) Synthesis, characterization, and microwave absorption properties of

- reduced graphene oxide/strontium ferrite/polyaniline nanocomposites. *Nanoscale Res Lett* 11:141
- [18] Lv HL, Guo YH, Yang ZH, Cheng Y, Wang LY, Zhang BS, Zhao Y, Xu ZCJ, Ji GB (2016) A brief introduction to the fabrication and synthesis of graphene based composites for the realization of electromagnetic absorbing materials. *J Mater Chem C* 5:491–512
- [19] Cao MS, Chen H, Wang XX, Zhang M, Zhang YL, Shu JC, Yang HJ, Fang XY, Yuan J (2018) Graphene nanohybrids: excellent electromagnetic properties for the absorbing and shielding of electromagnetic waves. *J Mater Chem C* 6:4586–4602
- [20] Lai YR, Wang SY, Qian DL, Zhong ST, Wang YP, Han SJ, Jiang W (2017) Tunable electromagnetic wave absorption properties of nickel microspheres decorated reduced graphene oxide. *Ceram Int* 43:12904–12914
- [21] Ma J, Wang XX, Cao WQ, Han C, Yang HJ, Yuan J, Cao MS (2018) A facile fabrication and highly tunable microwave absorption of 3D flowerlike Co_3O_4 -rGO hybrid-architectures. *Chem Eng J* 339:487–498
- [22] Hummers WS, Offeman RE (1958) Preparation of graphitic oxide. *J Am Chem Soc* 80:1339
- [23] Bhattacharya P, Dhibar S, Hatui G, Mandal A, Das T, Das CK (2014) Graphene decorated with hexagonal shaped M-type ferrite and polyaniline wrapper: a potential candidate for electromagnetic wave absorbing and energy storage device applications. *RSC Adv* 4:17039–17053
- [24] Wang Y, Wu XM, Zhang WZ, Huang S (2015) Facile synthesis of Ni/PANI/RGO composites and their excellent electromagnetic wave absorption properties. *Synth Metals* 210:165–170
- [25] Baniasadi A, Ghasemi A, Nemati A, Ghadikolaei MA, Paimozd E (2014) Effect of Ti–Zn substitution on structural, magnetic and microwave absorption characteristics of strontium hexaferrite. *J Alloys Compd* 583:325–328
- [26] Li M, Huang XY, Wu C, Xu HP, Jiang PK, Tanaka T (2012) Fabrication of two-dimensional hybrid sheets by decorating insulating PANI on reduced graphene oxide for polymer nanocomposites with low dielectric loss and high dielectric constant. *J Mater Chem* 22:23477–23484
- [27] Sawangphruk M, Suksomboon M, Kongsupornsak K, Khuntilo J, Srimuk P, Sanguansak Y, Klunbud P, Suktha P, Chiochan P (2013) High-performance supercapacitors based on silver nanoparticle-polyaniline-graphene nanocomposites coated on flexible carbon fiber paper. *J Mater Chem A* 1:9630–9636
- [28] Luo JH, Zuo Y, Shen P, Yan Z, Zhang K (2017) Excellent microwave absorption properties by tuned electromagnetic parameters in polyaniline-coated $\text{Ba}_{0.9}\text{La}_{0.1}\text{Fe}_{11.9}\text{Ni}_{0.1}\text{O}_{19}$ /reduced graphene oxide nanocomposites. *RSC Adv* 7:36433–36443
- [29] Sözeri Hüseyin, Mehmedi Z, Kavas Hüseyin, Baykal Abdülhadi (2015) Magnetic and microwave properties of $\text{BaFe}_{12}\text{O}_{19}$ substituted with magnetic, non-magnetic and dielectric ions. *Ceram Int* 41:9602–9609
- [30] Xu Y, Yang GL, Chu DP, Zhai HR (1990) Theory of the single ion magnetocrystalline anisotropy of 3D ions. *Phys Status Solidi B* 157:685–693
- [31] Wen B, Cao MS, Lu MM, Cao WQ, Shi HL, Liu J, Wang XX, Jin HB, Fang XY, Wang WZ, Yuan J (2014) Reduced graphene oxides: light-weight and high-efficiency electromagnetic interference shielding at elevated temperatures. *Adv Mater* 26:3484–3489
- [32] Wang TS, Liu ZH, Lu MM, Wen B, Ouyang QY, Chen YJ, Zhu CL, Gao P, Li CY, Cao MS, Qi LH (2013) Graphene- Fe_3O_4 nanohybrids: synthesis and excellent electromagnetic absorption properties. *J Appl Phys* 113:024314
- [33] Feng W, Wang YM, Chen JC, Wang L, Guo LX, Ouyang JH, Jia DC, Zhou Y (2016) Reduced graphene oxide decorated with in situ growing ZnO nanocrystals: facile synthesis and enhanced microwave absorption properties. *Carbon* 108:52–60
- [34] Panwar V, Mehra RM (2010) Analysis of electrical, dielectric, and electromagnetic interference shielding behavior of graphite filled high density polyethylene composites. *Polym Eng Sci* 48:2178–2187
- [35] Liu XG, Wu ND, Cui CY, Bi NN, Sun YP (2015) One pot synthesis of $\text{Fe}_3\text{O}_4/\text{MnO}_2$ core-shell structured nanocomposites and their application as microwave absorbers. *RSC Adv* 5:24016–24022
- [36] Zong M, Huang Y, Zhao Y, Sun X, Qu CH, Luo DD, Zheng JB (2013) Facile preparation, high microwave absorption and microwave absorbing mechanism of RGO- Fe_3O_4 composites. *RSC Adv* 3:23638–23648
- [37] Zhou W, Long L, Xiao P, Li Y, Luo H, Hua WD, Yin RM (2017) Silicon carbide nano-fibers in situ grown on carbon fibers for enhanced microwave absorption properties. *Ceram Int* 43:5628–5634
- [38] Fang J, Liu T, Chen Z, Wang Y, Wei W, Yue X, Jiang Z (2016) A wormhole-like porous carbon/magnetic particles composite as an efficient broadband electromagnetic wave absorber. *Nanoscale* 8:8899–8909
- [39] Wei X, Wang GS, Yin PG (2018) Designed fabrication of reduced graphene oxides/Ni hybrids for effective electromagnetic absorption and shielding. *Carbon* 139:759–767
- [40] Zhang XJ, Wang GS, Cao WQ, Wei YZ, Liang JF, Cao MS (2014) Enhanced microwave absorption property of reduced graphene oxide (RGO)- MnFe_2O_4 nanocomposites and

- polyvinylidene fluoride. *ACS Appl Mater Interfaces* 6:7471–7478
- [41] Cao MS, Wang XX, Cao WQ, Fang XY, Wen B, Yuan J (2018) Thermally driven transport and relaxation switching self-powered electromagnetic energy conversion. *Small* 14:1800987
- [42] Cao WQ, Wang XX, Yuan J, Wang WZ, Cao MS (2015) Temperature dependent microwave absorption of ultrathin graphene composites. *J Mater Chem C* 3:10017–10022
- [43] Wen B, Cao MS, Hou ZL, Song WL, Zhang L, Lu MM, Jin HB, Fang XY, Wang WZ, Yuan J (2013) Temperature dependent microwave attenuation behavior for carbon-nanotube/silica composites. *Carbon* 65:124–139